



Synthesis and study of the structure, magnetic, optical and methane gas sensing properties of cobalt doped zinc oxide microstructures

Z. Aghagoli¹ · M. Ardyanian¹

Received: 14 December 2017 / Accepted: 29 January 2018 / Published online: 6 February 2018
© Springer Science+Business Media, LLC, part of Springer Nature 2018

Abstract

Undoped and Cobalt (Co) doped zinc oxide (ZnO & CZx) nanoparticles were synthesized by Solvothermal method. The samples were studied by X-Ray Diffraction (XRD), Energy Dispersive X-ray Spectroscopy (EDS), Inductively Coupled Plasma Atomic Emission Spectroscopy (ICP-AES), UV–Vis spectroscopy and Scanning and Transmission Electron Microscopy (SEM & TEM). Moreover the gas sensing properties of the nanoparticles for methane gas took place. Purity of the samples and Co concentration was investigated by EDS and ICP spectroscopy respectively. XRD results described the hexagonal wurtzite structure for all the samples in which crystallinity and the crystallites size decreased with increase of Co doping level. Using UV–Vis spectroscopy the band gap energy was evaluated and redshift of band gap energy was observed by increasing of Co concentration. SEM images demonstrated that nanoparticles were agglomerated with increase of Co doping level. TEM images revealed the nanoparticles size in the range 11–44 nm. Methane sensing properties was enhanced after Co doping of the ZnO nanoparticles for Co concentration up to 4%.

1 Introduction

Methane (CH₄) is an organic gas which is used in various domains as industry and domestic applications, for example in hydrogen and ethylene production, [1, 2]. Heating and cooking [3, 4] etc. Since methane is a highly volatile gas in nature, it is explosive when mixed with air down to about 5% of concentration [4, 5]. Moreover methane is abundant gas in the coal mines, so its monitoring in low parts (ppb) concentration level in the air by gas sensor is an important subject to avoid the accidental explosion in the coal mines and industrial sites.

In the last decades the nanostructures and nanocomposites have attracted the researchers attention because of their potential applications in various scientific and industrial domains. For example photocatalytic application for air pollution prevention [6–10], gas sensor applications [11, 15], and photoluminescence effect [12, 13]. Between the various compounds, zinc oxide (ZnO) nanostructures are well candidates for many applications because of their direct band gap ($E_g = 3.37$ eV), high transparency, large exciton binding

energy (60 meV), good thermal stability, biocompatibility and high electron mobility [11–13]. These favorable properties and mature growth and easy preparation methods leads to construct functional of ZnO-based devices; for example field-effect transistors, light emitters, lasers, solar cells and gas sensors [14–21].

Recently, great efforts were effectuated to fabricate the efficient methane sensor based on indium and Zinc oxide [22, 23, 28]. ZnO doping changes its electrical, magnetic and sensing properties greatly [23–25], so the efforts for gas sensor fabricating were based on thermal conductivity, IR absorption, optical interferometry, and so on [22, 23]. Sun et al. achieved to methane detection response of 500 ppm with response time about 30 s by fabricating a gas sensor based on four-filament thermal conductivity [26, 28]. Li et al. fabricated a hybrid micro-sensor based on rhodium oxide/alumina with the response time less than 9 s and pre-alarm concentration 10% lower than explosion limit [27]. Various researchers groups reported their results about improve of the methane sensing properties of ZnO [28–31]. Hu et al. fabricated the methane sensors based on Co doped ZnO microstructures using hydrothermal method with response time about 19 s for methane concentration down to 100 ppm [28]. Their results were compared with the results of Basu et al. [29, 30] and Chen et al. [32] that fabricated methane sensors based on ZnO thin films and ZnO nanowalls respectively [28] researching the

✉ M. Ardyanian
ardyanian@du.ac.ir

¹ School of Physics and Center for Solid State Physics Research, Damghan University, Damghan 36716-41167, Iran

facile synthesis method, Pal et al. synthesized Co doped ZnO microstructures by solvothermal method, while they didn't investigated the methane sensor properties [33]. In this work ZnO and Co doped ZnO (CZx) nanoparticles were synthesized by facile solvothermal method. Then the structure, optical, magnetic and methane sensor properties of the samples were investigated. Finally the best efficiency of gas sensor was determined as a function of Co concentration, work temperature and gas concentration.

2 Experimental details

2.1 Synthesis of ZnO microstructures

Synthesis of ZnO and CZx nanoparticles (nps) was carried out using solvothermal method. The solution was prepared by dissolving the mixture of Zinc nitrate hexa-hydrate (0.10 mol, $Zn(NO_3)_2 \cdot 6H_2O$) and oxalic acid di-hydrate (0.15 mol, $C_2H_2O_4 \cdot 2H_2O$) as complexing agent in 100 ml of distilled deionized water. For Co doping, Cobalt nitrate hexa-hydrate ($CoNO_3 \cdot 6H_2O$) was added to the initial solution and stirred for 30 min at 45 °C by magnetic stirrer. The Co/Zn weight ratio was $x=0.5, 1, 3$ and 5 wt%. Based on Co concentration the samples were labeled as CZ0.5, CZ1, CZ3 and CZ5 respectively. Subsequently, the solution was refluxed at 75 °C for 15 h and heated at 90 °C for 10 h in oil bath. Finally, after sintering at 130 °C for 2 h, the white powder of ZnO and green powder of CZx were obtained.

2.2 Characterization

Structure and crystallographic phase of the samples were studied by XRD technique. The XRD patterns were recorded on a Bruker D8 Advance diffractometer (40 kV–40 mA, Cu K α radiation, $\lambda=0.15406$ nm). Diffractograms were recorded in the range of $2\theta=10^\circ-80^\circ$ with a step size of 0.02° . The crystallites size was estimated employing Scherrer equation [34]:

$$D = \frac{k\lambda}{\beta \cos \theta} \quad (1)$$

in which D is the crystallites size, k is Scherrer shape factor and about 0.9 for spherical particles, β is the line broadening at Full Width at Height Maximum (FWHM), λ is the wavelength of the X-ray beam and θ is the diffraction angle (peak position). The Bragge planes distance (d) was calculated by following equation [30]:

$$\frac{1}{d_{hkl}^2} = \frac{4}{3} \frac{(h^2 + hk + k^2)}{a^2} + \frac{l^2}{c^2} \quad (2)$$

in which a and c are the lattice constants, l is the bond length, and d_{hkl} is the distance of the hkl Bragge plane which obtains from Bragge equation:

$$2d \sin \theta_{hkl} = n\lambda_{hkl} \quad (3)$$

The lattice constants were calculated using the following equations [35]:

$$a = \frac{\lambda}{\sqrt{3} \sin \theta_{100}} \quad (4)$$

$$c = \frac{\lambda}{\sin \theta_{002}} \quad (5)$$

As it is seen in Table 1, the lattice constants in Co doped samples haven't significant change, which is attributed to substitution of Zn^{2+} by Co^{2+} ions.

The bond length (l) and the volume of unit cell for ZnO were calculated by following equations [35]:

$$l = \sqrt{\frac{a^2}{3} + \left(\frac{1}{2} - u\right)^2 \times c^2} \quad (6)$$

in which u is related to peak situation and was calculated by [35]:

$$u = \frac{a^2}{3c} + 0.25 \quad (7)$$

The volume of unit cell was also calculated by the next equation [35]:

$$V = 0.866 \times (a^2) \times c \quad (8)$$

The microstrain was calculated by Eq. (9) [36]

$$\epsilon = \frac{\beta \cos \theta}{4} \quad (9)$$

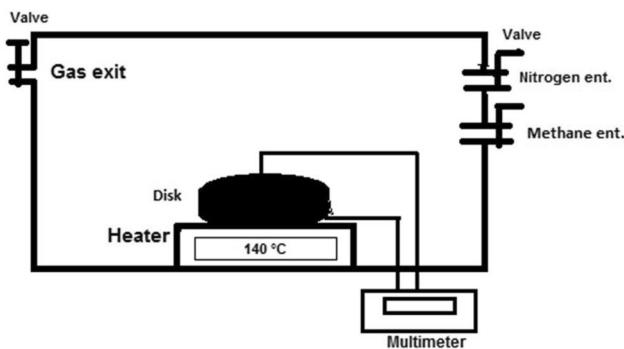
In which β is the line broadening at Full Width at Height Maximum (FWHM) and θ is the diffraction angle (peak position).

Co molar concentration was measured by inductively coupled plasma atomic emission spectroscopy (ICP-AES) model GBC integra XL. The shape, size and morphology of the nanoparticles were investigated by transmission electron microscopy (TEM, CM30 300 kV), and scanning electron microscopy (SEM HITACH S-4160) respectively. Elemental analysis was performed by energy dispersive spectroscopy (EDS) integrated into the SEM system. Absorbance measurements were carried out by UV-Vis spectrophotometer model Unico 4802 double-beam in the range of 190–1100 nm, using dispersed nps in alcohol. The absorption coefficient was obtained using the following equation [34]:

$$\alpha = 2.303 \frac{A}{t} \quad (10)$$

Table 1 XRD parameters of CZx microstructures for three strongest peaks and different Co concentration

Sample	hkl	2θ	FWHM	d (Å)	ε	D (nm)	a (Å)	c (Å)	l (Å)	V (Å ³)
ZnO	101	36.28	0.577	2.47	0.137	18	3.24	5.20	1.974	47.40
	100	31.82	0.492	2.83	0.118					
	002	34.45	0.502	2.60	0.119					
CZ0.5	101	36.24	0.692	2.48	0.164	15	3.25	5.20	1.975	47.45
	100	31.77	0.598	2.82	0.143					
	002	34.44	0.604	2.61	0.144					
CZ1	101	36.30	0.694	2.47	0.164	15	3.24	5.20	1.976	47.48
	100	31.84	0.589	2.81	0.141					
	002	34.45	0.554	2.60	0.132					
CZ3	101	36.30	0.723	2.47	0.171	13	3.24	5.20	1.976	47.52
	100	31.84	0.596	2.81	0.143					
	002	34.44	0.651	2.61	0.155					
CZ5	101	36.26	0.771	2.47	0.183	13	3.25	5.21	1.977	47.56
	100	31.80	0.656	2.82	0.157					
	002	34.43	0.712	2.61	0.170					

**Fig. 1** A schematic image of gas sensing setup

in which A is the absorbance and t is the mean nps diameter.

The band gap energy of the samples was also obtained by extrapolating of the curve of the tauc equation for direct band gap [34]:

$$(\alpha h\nu)^2 = A(h\nu - E_g) \quad (11)$$

Magnetic properties of the samples were studied by vibrating sample magnetometer (VSM) model Lake shore 7400 with a 1.8 T magnetic field.

2.3 Fabrication and measurements of sensors

For sensor measurements, the discs of 12 mm diameter and 2.5 mm thickness containing 0.8 g of CZx nanopowder were fabricated by pressing under 30 Mpa pressure and calcined at 500 °C. Ohmic electrical contacts on the discs were made using Silver glue, followed by heating between 120 and 150 °C for stabilizing the ohmic contacts. Figure 1 represents a schematic image of the utilized experimental set

up for methane sensing measurements. The discs were put into an evacuated chamber on the hot plate kept at 140 °C. Nitrogen was entered in the chamber for neutering of the chamber atmosphere. After stabilizing of the disk resistance, specified dose of Methane was entered in the chamber. Due to reaction between methane and the disc, resistance varies. After stabilizing of the resistance value, the final resistance was recorded.

3 Results and discussion

3.1 EDS and ICP results

Figure 2 represents the elemental analysis results that was performed by EDS spectroscopy for CZ1 and CZ3 samples. In spite of strong and so near $L\alpha$ peaks, $K\alpha$ peaks of Zn, O and Co species are not so obvious. While the results confirm the purity of the microstructures. ICP spectroscopy was also effectuated for determining the precise Co molar concentration. A solution of CZ1 and CZ3 samples in nitric acid was prepared for breaking the chemical bonds and separating of Co^{2+} and Zn^{2+} ions. Figure 3 shows the emitted spectra corresponding to Co^{2+} and Zn^{2+} ions. Calculation of the ratio of the area under the curves, results in molar ratio of $[Co]/[Zn]$ which was found as 0.7 and 2.6% for CZ1 and CZ3 samples respectively and in accordance with their mass concentration (x value).

3.2 XRD results

Figure 4 represents the XRD results of CZx nps as a function of Co concentration. The XRD pattern showed that all the samples exhibited the hexagonal wurtzite structure (JCPDS

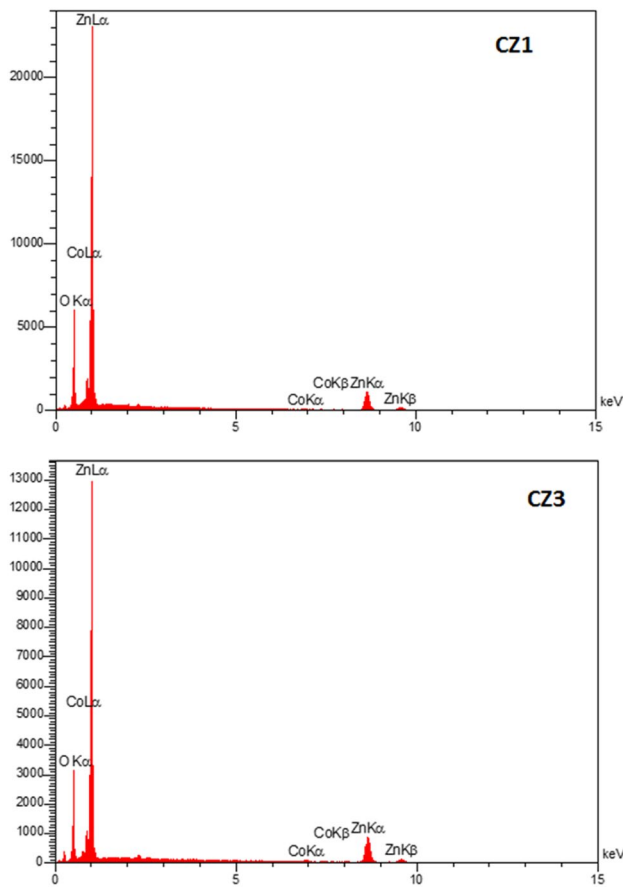


Fig. 2 EDS spectroscopy results for CZ1 and CZ3 samples

NO: 036-1451). The peaks at 31.84° , 34.40° , 36.28° , 47.56° , 56.6° , 62.88° , 66.56° , 67.92° , 69.12° , 72.52° , are attributed to (100), (002), (101), (103), (200), (112), (201), (004), planes respectively. The preferred orientation was found at [101]. The symmetry group was P63mc and the lattice parameters were found $a = b = 3.2498$, $C = 5.2066$. In this work the [100], [101] and [002] were considered as preferred orientations and their corresponding planes are under investigation and their structural parameters were represented in Table 1. It is seen that nanocrystallites size (D) (see Eq. 1) decreased and microstrain (ϵ) (see Eq. 9) increased by increasing of Co content.

As it is seen in XRD pattern, the intensity of the peaks were generally reduced by increasing of Co concentration. Moreover contrary of the other reports [28], no other secondary phases, such as Co clusters or cobalt oxides. Similar results were also reported by other groups [37, 38] which indicates that the dopant Co^{2+} ions with ionic radius of 0.58 \AA are substituted in the inner lattice of Zn^{2+} ions with ionic radius of 0.6 \AA [39]. Small shift of diffraction peaks to higher angles and the peak broadening was observed by

increasing of Co content (see Table 1). Diffraction peak shift could be due to decrease of planes distance which is caused by the increase of microstrain after doping [40]. The peak broadening may be due to the size reduction and microstrain (see Table 1) [41] of CZ_x nps. Size reduction of the nps is also attributed to the distortion in the host ZnO lattice by the Co^{2+} ions; this leads to decrease of the nucleation and subsequent growth rate of ZnO nps [36]. Figure 5 represents a general increase of the unit cell volume and bond length by increasing of Co content (x value). Due to Co doping, the lattice constants varies and according to Vegard's law, higher Co content could to increase of the volume of the unit cell [36, 42].

3.3 Optical properties

Figure 6 represents the absorbance spectra of the dispersed nanoparticles in ethanol. As it is observed, a significant decrease is observed for absorbance of CZ1 nanoparticles with no significant shift in absorption edge. For higher x values, the absorbance increases and absorption edge has a redshift. Absorbance changes could be attributed to nanocrystallites size change in accordance with XRD results. Nanocrystallites size of CZ1 sample decreased significantly, and subsequently increased for higher x values (see Table 1). Redshift of absorption edge also could be attributed to band gap narrowing in CZ_x samples. This result was confirmed by the results of Figs. 7 and 8 containing direct band gap measurements. The band gap narrowing could also be attributed to sp - d exchange interaction between band electrons of ZnO and localized electrons in d orbitals of Co^{2+} ions. In fact interaction between s - d and p - d orbitals guides the positive and negative charges to conduction and valence bands edge which leads to reduction of band gap energy [36]. Anyway band gap narrowing is directly proportional to Co concentration which suggests the possibility of band gap engineering by controlling of Co concentration. The optical results suggest that Co doping doesn't change the ZnO structure confirming the XRD results [36]. In the literature, there are the reports concerning blueshift of the absorption edge in $\text{Co}:\text{ZnO}$ nanostructures and band gap energy increased from 3.33 (pure ZnO) to 4.13 eV (for 7% Co) [36]. The blueshift was attributed to active transitions involving 3d levels in Co^{2+} ions and strong sp - d exchange interactions between the itinerant 'sp' carriers (band electrons) and localized 'd' electrons of the dopant [43].

3.4 Microscopy images

SEM and TEM images are represented in Figs. 9 and 10 respectively. SEM images describe that ZnO microstructures have quasi-spherical shape with diameter around $1.5 \mu\text{m}$. In

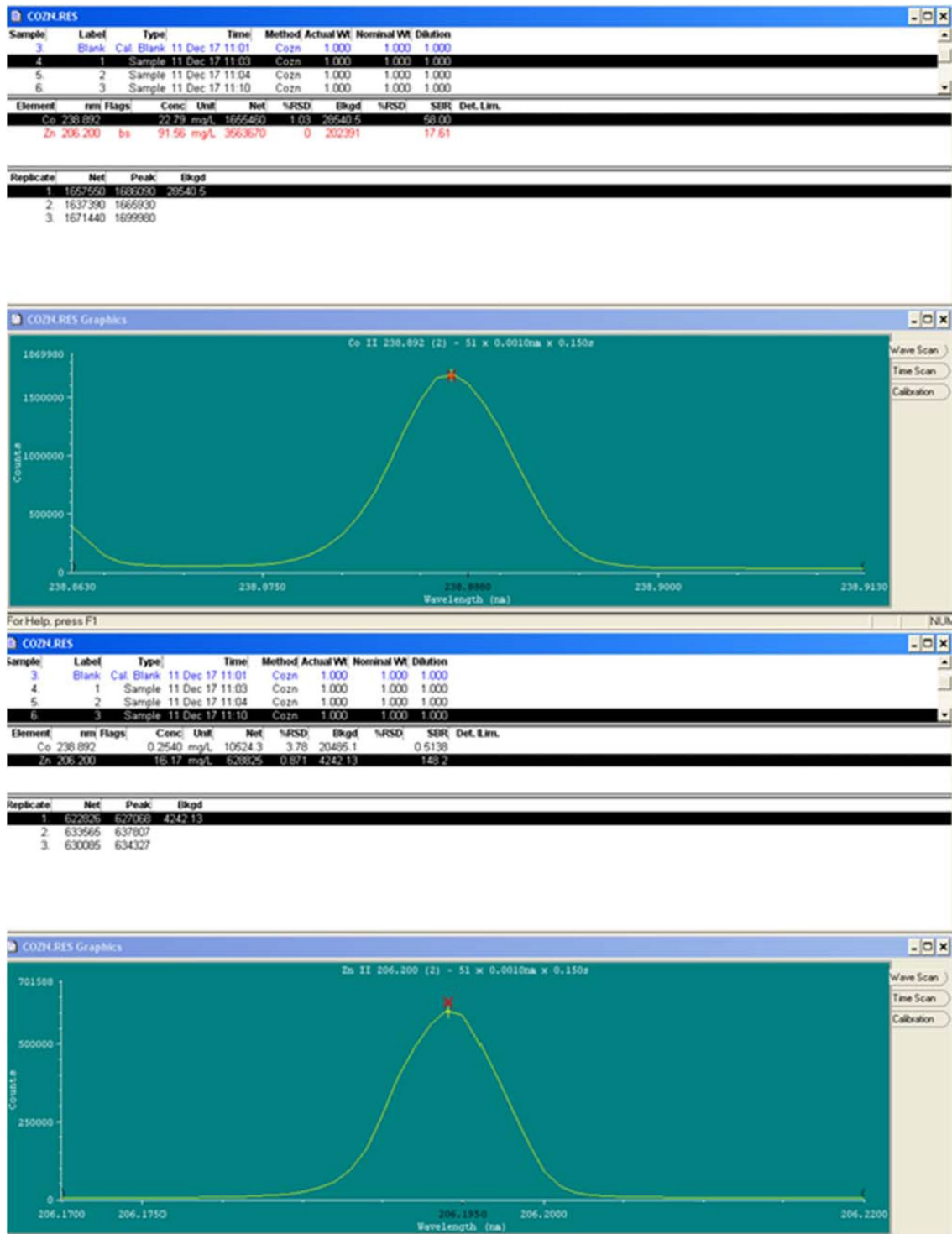


Fig. 3 ICP spectra of Co (up) and Zn (down) and their concentration in CZ1 sample

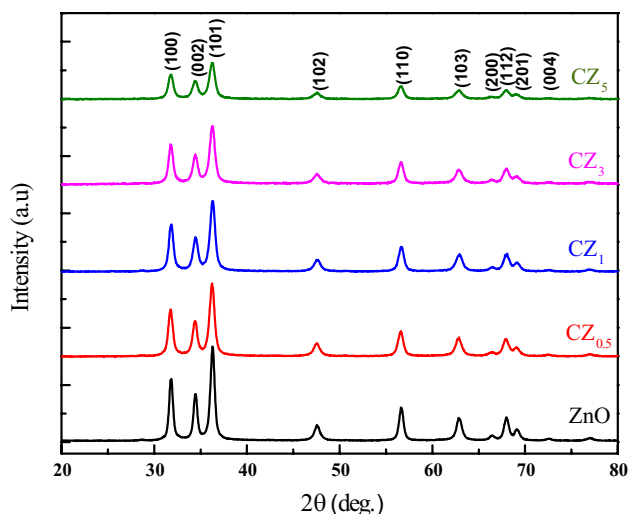


Fig. 4 The XRD pattern of CZ_x microstructures as a function of Co concentration

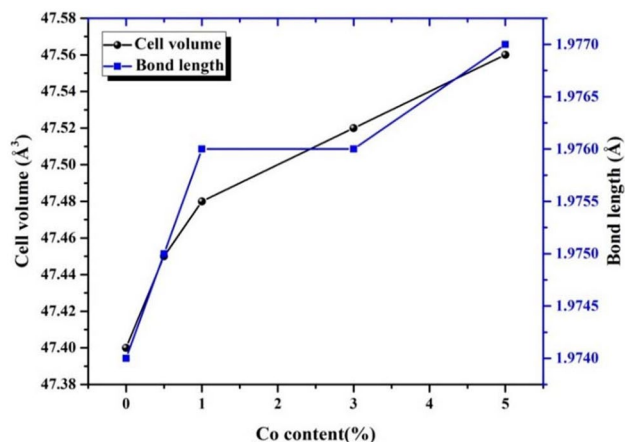


Fig. 5 Variations of the bond length and cell volume as a function of Co concentration

Co doped samples the microstructures get disorder shape. For higher Co content, the microstructures are more agglomerated and porosity increased. The TEM image represents the CZ1 nps. The nps diameter was found between 11 and 40 nm with hexagonal structure.

3.5 Magnetic properties

Figure 11 represents the hysteresis curve of the CZ1 sample. As it is observed, for Co concentration as 1%, ZnO represents ferromagnetic property. The narrow curve confirms that the sample is a soft ferromagnetic.

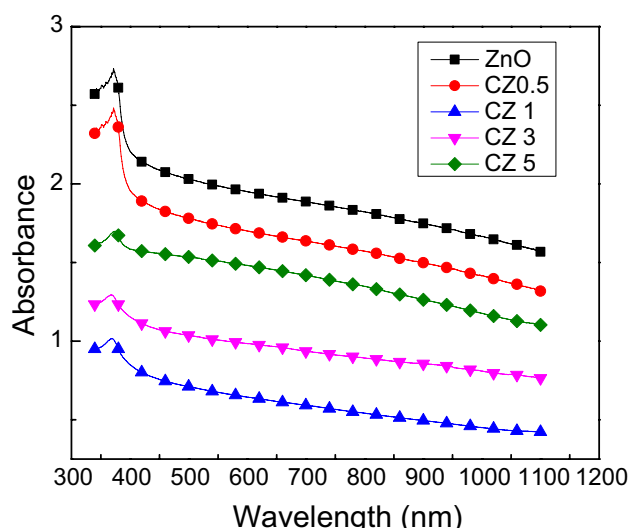


Fig. 6 Absorbance spectra of CZ_x samples as a function of Co content (x value)

The saturation magnetization (M_s), remained magnetization (M_r) and magnetic helicity (H_c) were found at 7.9285×10^{-3} (emu/g), 7.4165×10^{-3} (emu/g), and 81.762 G respectively. Theoretical studies suggested the transition metals doped are well candidate for room temperature ferromagnetism (RTFM). The ferromagnetism property was also reported for iron doped [44] and Co doped ZnO by other research groups [31]. For non-magnetic III–V or II–VI semiconductors, substitution of the cations by magnetic dopants as Mn, Fe, Co leads to produce of diluted Magnetic Semiconductor. Although the origin of the (RTFM) is under controversy, the last reports suggest that the oxygen vacancy have important role for magnetic properties [31].

3.6 Methane sensing measurements

Gas sensor properties of ZnO and CZ_x samples were studied using the experimental set up introduced in Sects. 2–3. Mechanism of methane sensing was well explained elsewhere [28]. In this work, the best sample for methane sensor applications were found CZ1 and CZ3. After a systematic study, the temperature of 140 °C was found as optimal operating temperature. Moreover response time of the samples was measured for different methane concentrations. Influence of Co doping onto methane sensing properties was investigated in Figs. 12 and 13. Response of the sensor was defined as R_a/R_g in which R_a is resistance of the sensor in the air and R_g is the resistance in the

Fig. 7 Extrapolation of the curve of $(ah\nu)^2$ versus $h\nu$ and bandgap of CZx samples as a function of Co content (x)

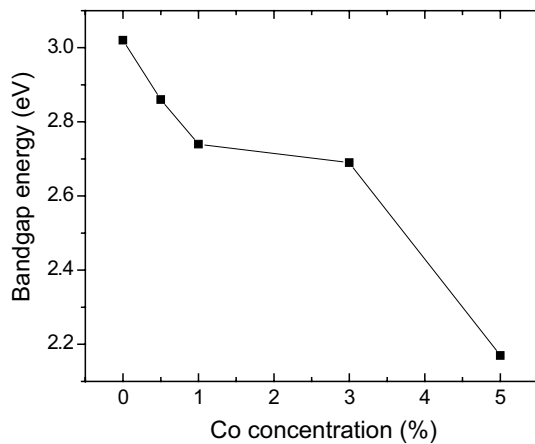
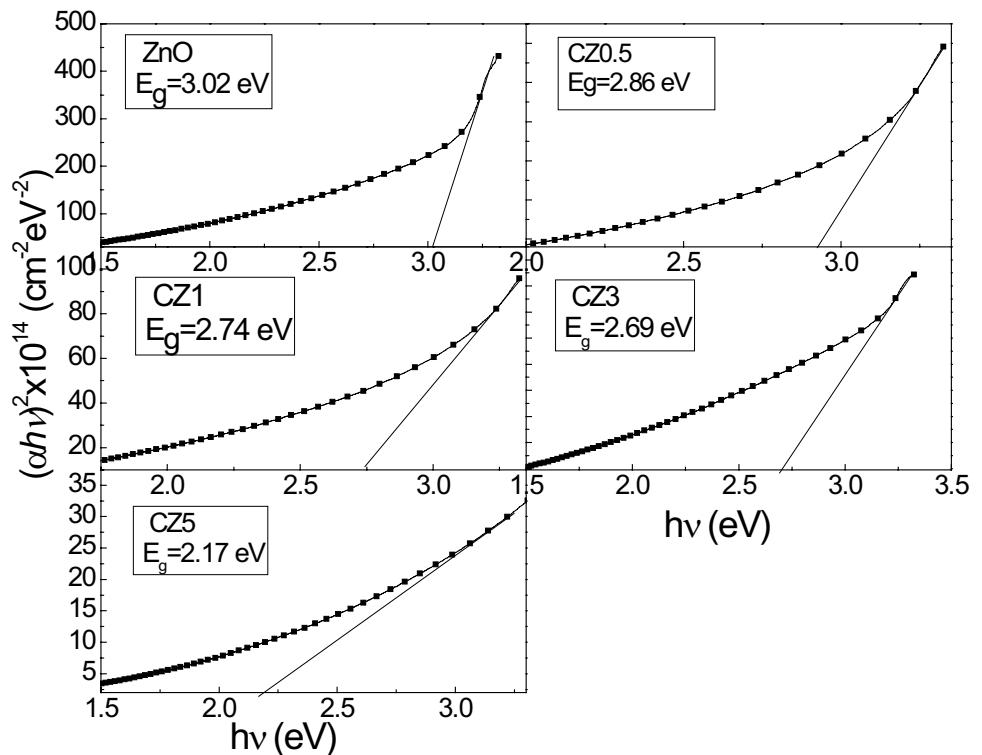


Fig. 8 Band gap variations of CZx nanoparticles versus Co concentration

gas. As it is observed in the Figs. 12 and 13 and Table 2. Comparing of the sensing parameters of CZx with ZnO samples at the same experimental conditions, describes that all of the parameters were modified after Co doping. Lowest response/recovery time at (25.2/6.6 s) was found in CZ3 sample for 100 PPM of methane at 140 °C. While

response value (1.10) of the CZ1 is the best between the others. A comparison of the methane sensor performance between present results and the other groups results [28] was represented in Table 2.

3.7 Methane sensing mechanism

As well discussed in the literature [28] pure ZnO gas sensor properties are based on the surface-adsorption of oxygen species [45, 46]. By exposing the n-type ZnO gas sensor to air, oxygen species can be absorbed onto its surface, this leads to formation of various anions as O_2^- , O^- , and O^{2-} , through capturing electrons from the conduction band (CB). So a depletion layer is formed near the ZnO surface. After exposing of the sensor in the atmosphere of a reducing gas as methane, the gas will react with ionic oxygen species and release the captured electrons back to the CB. This results in reduction of electrons in the depletion layer and contraction of electron transport potential barrier [11]. In Co doped ZnO (CZx) gas sensors, this mechanism is different, because p-type Co_3O_4 nanoparticles are attached on the surface of n-type ZnO microstructures. This leads to diffusion of electron-hole carriers in opposite directions similar to other p-n junctions and

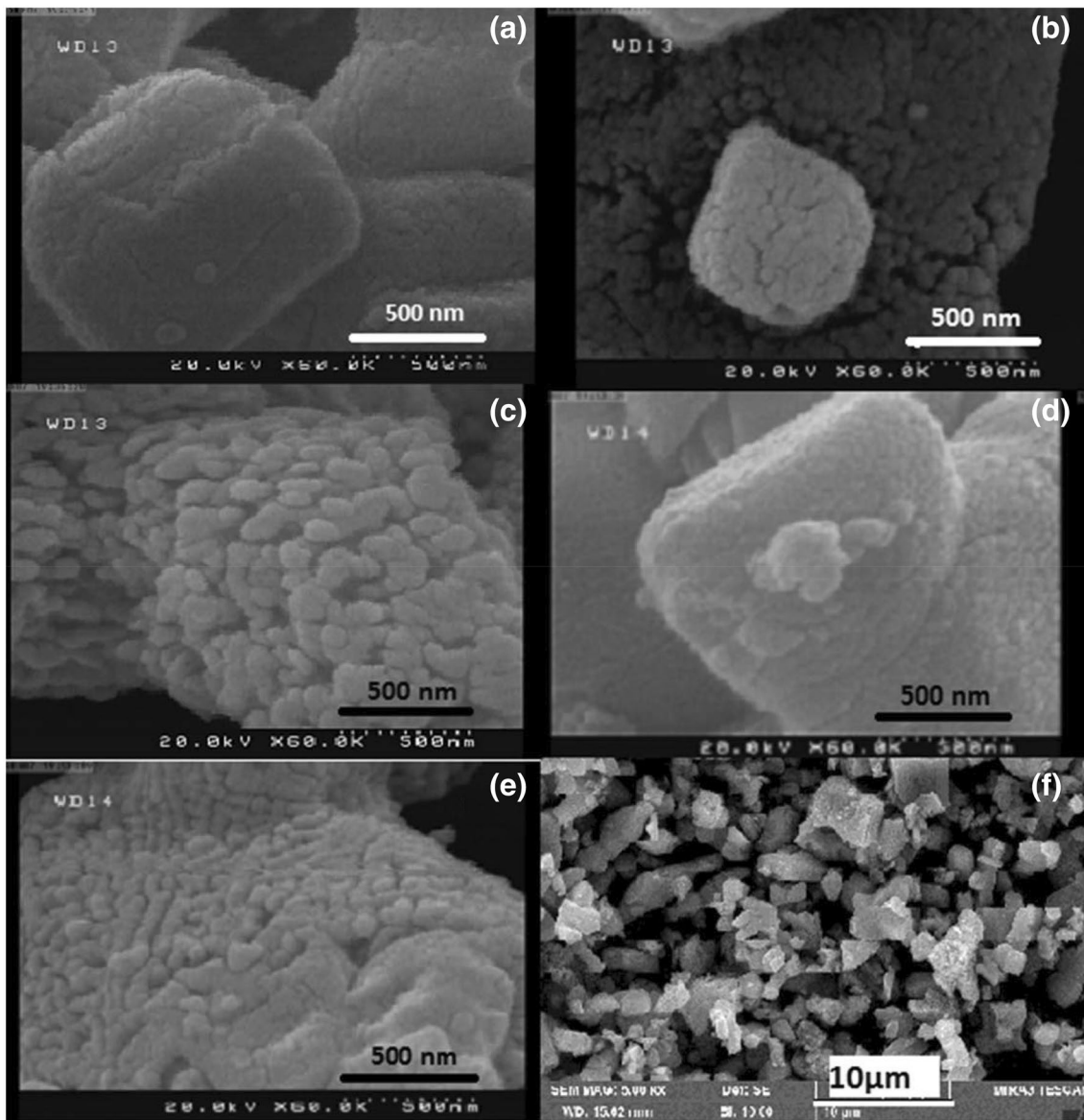


Fig. 9 SEM images of the CZ_x microstructures. **a** ZnO, **b** CZ0.5, **c** CZ1, **d** CZ3, **e** CZ5, **f** upward and low resolution image of CZ1

formation of internal electric field between their interface. This results in energy band bending in the depletion layer for equalizing the Fermi levels (E_F) and formation of P–n heterojunction. When CZ_x sensor is exposed to air, due to capture of electrons from CB and existence of potential barrier of depletion layer the resistance increases even higher than pure ZnO [47]. While exposed to methane gas the oxygen species react with methane molecules and release electrons into the CB which causes to decrease of resistance. Moreover methane gas releases

electrons to combine with holes in p-type Co_3O_4 . These phenomena lead to increase of electron concentration and decrease of hole concentration, which results in reduction of concentration gradient on both sides p–n heterojunction, diffusion of carriers is weakened and the potential barrier is decreased; therefore the resistance of gas sensor decreases. Based on above discussion, existing of Co_3O_4 phase is necessary for the explained reactions. Relating to synthesis method, if Co_3O_4 phase is observed in XRD patterns, it causes to increase the sensor performance [28].

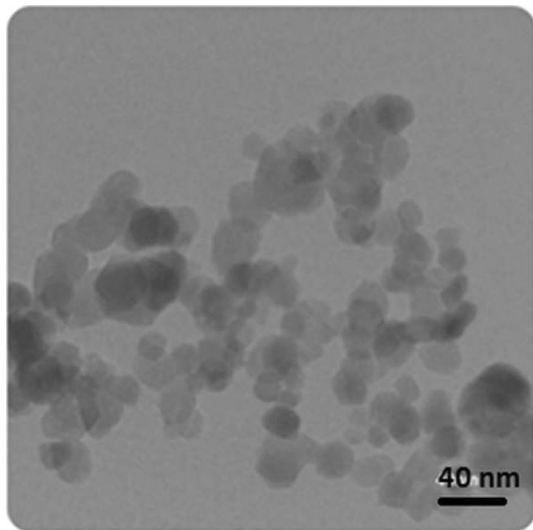


Fig. 10 TEM images of CZ1 nanoparticles

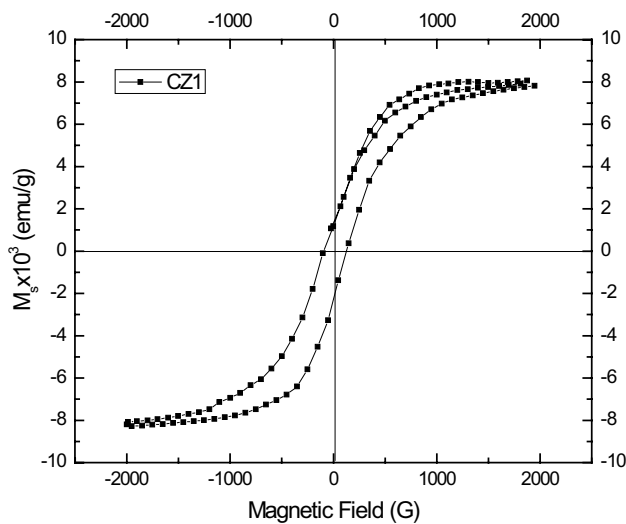


Fig. 11 Hysteresis curve of CZ1 microstructure

While in this work no trace of Co_3O_4 was observed, and so the mechanism of CZ_x methane sensors could not be valid for present work. As observed in Table 2, the performance of present CZ_x sensors is better than pure ZnO while not better than other groups CZ_x sensors [28]. It could be attributed to increase of the surface/volume ratio due to decrease of nanograins size (see Fig. 8) after Co doping which leads to increase of oxygen surface absorption also electrons in CB. It seems that well substituting

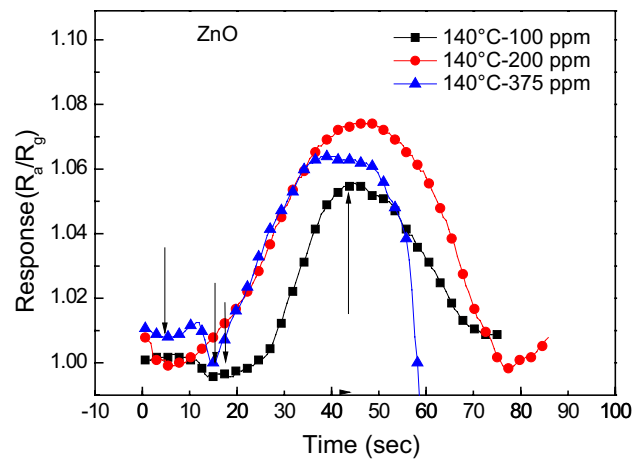


Fig. 12 Response of ZnO gas sensor for different Methane concentrations

of Co^{2+} ions in the inner lattice of the Zn^{2+} ions is not an advantage for gas sensor applications and Co_3O_4 phase is necessary which depends on synthesis method. In spite of facility of solvothermal method and well quality of the structure and ferromagnetism property, methane sensing properties aren't extraordinary comparing the other synthesis methods [30, 36].

4 Conclusions

In this work Co doped ZnO microstructures were prepared by solvothermal method. XRD results showed the Hexagonal wurtzite structure with preferred orientation along [101]; the bond length and cell volume increased by increasing of Co content. Moreover no Co trace was found in XRD pattern which was attributed to well substitution of Co^{2+} ions in the inner lattice of the Zn^{2+} ions due to their close ionic radius. $[\text{Co}]/[\text{Zn}]$ molar ratio was measured by ICP spectroscopy for CZ1 and CZ3 samples as 0.7 and 2.6% respectively. Significant band gap energy reduction was observed for CZ_x samples ($x \geq 0.5$) which was attributed to sp-d exchange interaction between bond electrons of ZnO and localized electrons in d orbitals of Co^{2+} ions. Methane sensing results described the increase of sensor performance after Co doping the. Optimal sensor response and response time was found in the CZ3 sensor for 100 ppm of methane concentration at 140 °C. Since no trace of Co_3O_4 was found in XRD results, enhancement of sensor properties was attributed to increase of surface/volume ratio after doping.

Fig. 13 Response of CZ1 (a) and CZ3 (b) gas sensors for different Methane concentrations

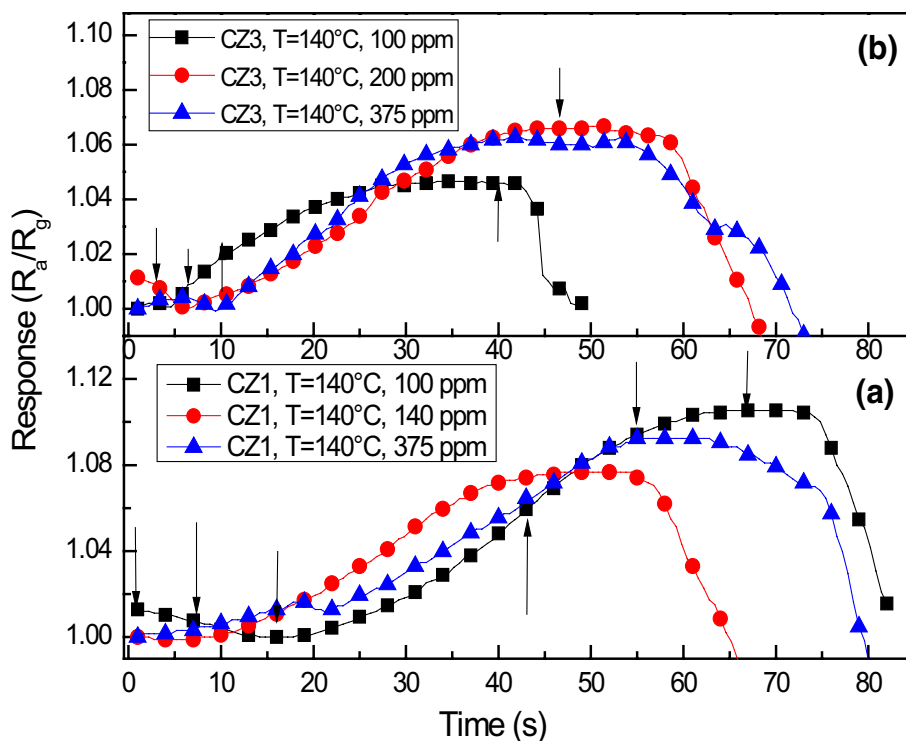


Table 2 Performance comparison of various methane gas sensors

Sensing material	Concentration (ppm)	Operating temperature (°C)	Response (R_a/R_g)	Resp/Rec. time (s)
ZnO thin film [29]	100	220	2.22	130.2/148.3
ZnO nanowalls [32]	100	300	2	6/21
ZnO microstruct. (present work)	100	140	1.054	39.5/27
	375	140	1.063	32.2/30.6
CZ1 mic.struct [28]	100	140	3.55	19/27
CZ1 (present work)	100	140	1.10	36/20.6
	375	140	1.07	26.8/23.4
CZ3 (present work)	100	140	1.047	25.2/6.6
	375	140	1.063	30.6/22.8

Acknowledgements This work was supported by the Research Council of Damghan University in I. R. Iran; the authors thanks Mr. A. Daryani and Mr. H. Azimi Jouybari for assisting during this project, Dr. M. Amiri for ICP and Dr. A. Gholizadeh for his helpful discussing about XRD results.

References

1. A.A. Al-Hassani, H.F. Abbas, W.M.A.W. Daud, Hydrogen production via decomposition of methane over activated carbons as catalysts: full factorial design. *Int. J. Hydrog. Energy* **39**, 7004–7014 (2014)
2. J. Shan, W. Huang, L. Nguyen, Y. Yu, S. Zhang, Y. Li, A.I. Frenkel, F. Tao, Conversion of methane to methanol with a bent mono (μ -oxo) dinickel anchored on the internal surfaces of microspores. *Langmuir* **30**, 8558–8569 (2014)
3. W. Eugster, G.W. Kling, Performance of a low-cost methane sensor for ambient concentration measurements in preliminary studies. *Atmos. Meas. Technol.* **5**, 1925–1934 (2012)
4. N.M. Vuong, N.M. Hieu, H.N. Hieu, H. Yia, D. Kim, Y. Han, M. Kimb, Ni_2O_3 -decorated SnO_2 particulate films for methane gas sensors. *Sens. Actuators B* **192**, 327–333 (2014)
5. J. Shen, T.J. Algeo, Q. Feng, L. Zhou, L. Feng, N. Zhang, J. Huang, Volcanically induced environmental change at the permian-triassic boundary: related to west siberian coal-field methane releases? *J. Asian. Earth Sci.* **75**, 95–109 (2013)
6. S. Zinatloo-Ajabshir, M. Salavati-Niasari, Facile route to synthesize zirconium dioxide (ZrO_2) nanostructures: structural, optical and photocatalytic studies. *J. Mol. Liq.* **216**, 545–551 (2016)
7. S. Zinatloo-Ajabshir, S. Mortazavi-Derazkola, M. Salavati-Niasari, Nd_2O_3 - SiO_2 nanocomposites: a simple sonochemical

- preparation, characterization and photocatalytic activity. *Ultrason. Sonochem.* **42**, 171–182 (2018)
8. Z. Salehi, S. Zinatloo-Ajabshir, M. Salavati-Niasari, Novel synthesis of $\text{Dy}_2\text{Ce}_2\text{O}_7$ nanostructures via a facile combustion route. *RSC Adv.* **6**, 26895–26901 (2016)
 9. S. Zinatloo-Ajabshir, M. Salavati-Niasari, Preparation of nanocrystalline cubic ZrO_2 with different shapes via a simple precipitation approach. *J. Mater. Sci.* **27**:3918–3928 (2016). <https://doi.org/10.1007/s10854-015-4243-1>
 10. S. Zinatloo-Ajabshir, M. Salavati-Niasari, Z. Zinatloo-Ajabshir, $\text{Nd}_2\text{Zr}_2\text{O}_7\text{-Nd}_2\text{O}_3$ nanocomposites: new facile synthesis, characterization and investigation of photocatalytic behaviour. *Mater. Lett.* **180**, 27–30 (2016)
 11. A. Wei, L. Pan, W. Huang, Recent progress in the ZnO nanostructure-based sensors. *Mater. Sci. Eng. B* **176**, 1409–1421 (2011)
 12. A.P. de Moura, R.C. Lima, M.L. Moreira, D.P. Volanti, J.W.M. Espinosa, M.O. Orlandi, P.S. Pizani, J.A. Varela, E. Longo, ZnO architectures synthesized by a microwave-assisted hydrothermal method and their photoluminescence properties. *Solid State Ion.* **181**, 775–780 (2010)
 13. J. Kennedy, P.P. Murmu, E. Manikandan, S.Y. Lee, Investigation of structural and photoluminescence properties of gas and metal ions doped zinc oxide single crystals. *J. Alloy Compd.* **616**, 614–617 (2014)
 14. H. Gullapalli, V.S.M. Vemuru, A. Kumar, A. Botello-Mendez, R. Vajtai, M. Terrones, S. Nagarajah, P.M. Ajayan, Flexible piezoelectric ZnO–paper nanocomposite strain sensor. *Small* **6**, 1641 (2010)
 15. V. Pachauri, A. Vlandas, K. Kern, K. Balasubramanian, Site-specific self-assembled liquid-gated ZnO nanowire transistors for sensing applications. *Small* **6**, 589 (2010)
 16. X. Fang, Y. Bando, U.K. Gautam, T. Zhai, H. Zeng, X. Xu, M. Liao, D. Golberg, *Crit. Rev. Solid State Mater. Sci.* **34**, 190 (2009)
 17. Q.F. Zhang, C.S. Dandeneau, X.Y. Zhou, G.Z. Cao, *Adv. Mater.* **21**, 4087 (2009)
 18. V. Postica, J. Gröttrup, R. Adelung, O. Lupan, A.K. Mishra, N.H. de Leeuw, N. Ababii, J.F.C. Carreira, J. Rodrigues, N.B. Sedrine, M.R. Correia, T. Monteiro, V. Sontea, Y.K. Mishra, A case study of the effects of metal doping on ZnO tetrapods with bismuth and tin oxides. *Adv. Funct. Mater.* **27**, 1604676 (2017)
 19. B. Zhao, F. Wang, H. Chen, L. Zheng, L. Su, D. Zhao, X. Fang, An ultrahigh responsivity (9.7 mA W^{-1}) self-powered solar-blind photodetector based on individual ZnO– Ga_2O_3 heterostructures. *Adv. Funct. Mater.* **27**, 1700264 (2017)
 20. W. Lu, D. Zhu, X. Xiang, Synthesis and properties of Ce-doped ZnO as a sensor for 1,2-propanediol. *J. Mater. Sci.* **28**, 18929–18935 (2017)
 21. K. Lokesh, G. Kavitha, E. Manikandan, G.K. Mani, K. Kaviyarasu, J.B.B. Rayappan, R. Lachumananandasivam, J.S. Aanand, M. Jayachandran, M. Maaza, Effective ammonia detection using n-ZnO/p-NiO heterostructured nanofibers. *IEEE Sens. J.* **16** 2477–2483 (2016)
 22. N.M. Vuong, N.M. Hieu, D. Kim, B.I.I. Choi, M. Kim, Ni_2O_3 decoration of In_2O_3 nanostructures for catalytically enhanced methane sensing. *Appl. Surf. Sci.* **317**, 765–770 (2014)
 23. Y.C. Liang, H.Y. Hsia, Y.R. Cheng, C.M. Lee, S.L. Liu, T.Y. Lin, C.C. Chung, Crystalline quality-dependent gas detection behaviors of zinc oxide-zinc chromite p-n heterostructures. *CrystEngComm* **17**, 4190–4199 (2015)
 24. J. Pivin, G. Socol, I. Mihailescu, P. Berthet, F. Singh, M. Patel, L. Vincent, Structure and magnetic properties of ZnO films doped with Co, Ni or Mn synthesized by pulsed laser deposition under low and high oxygen partial pressures. *Thin Solid Films* **517**(2), 916–922 (2008)
 25. N.F. Djaja, D.A. Montja, R. Saleh, The effect of Co incorporation into ZnO nanoparticles. *Adv. Mater. Phys. Chem.* **3**, 33–41 (2013)
 26. J. Sun, D. Cui, X. Chen, L. Zhang, H. Cai, H. Li, Design, modeling, microfabrication and characterization of novel micro thermal conductivity detector. *Sens. Actuators B* **160**, 936–941 (2011)
 27. L. Li, S. Niu, Y. Qu, Q. Zhang, H. Li, Y. Li, W. Zhao, J. Shi, One-pot synthesis of uniform mesoporous rhodium oxide/alumina hybrid as high sensitivity and low power consumption methane catalytic combustion micro-sensor. *J. Mater. Chem.* **22**, 9263–9267 (2012)
 28. J. Hu, F. Gao, Z. Zhao, S. Sang, P. Li, W. Zhang, X. Zhou, Y. Chen, Synthesis and characterization of cobalt-doped ZnO microstructures for methane gas sensing. *Appl. Surf. Sci.* **363**, 181–188 (2016)
 29. P.K. Basu, P. Bhattacharyya, N. Saha, H. Saha, S. Basu, The superior performance of the electrochemically grown ZnO thin films as methane sensor. *Sens. Actuators B* **133**, 357–363 (2008)
 30. P.K. Basu, S.K. Jana, H. Saha et al., Low temperature methane sensing by electrochemically grown and surface modified ZnO thin films. *Sens. Actuators B* **135**(1), 81–88 (2008)
 31. B. Pal, P.K. Giri, High temperature ferromagnetism and optical properties of Co doped ZnO nanoparticles. *J. Appl. Phys.* **108**, 084322 (2010)
 32. T.P. Chen, S.P. Chang, F.Y. Hung, S.J. Chang, Z.S. Hu, K.J. Chen, Simple fabrication process for 2D ZnO nanowalls and their potential application as a methane sensor. *Sensors* **13**, 3941–3950 (2013)
 33. B. Pal, S. Dhara, P.K. Giri, D. Sarkar, Room temperature ferromagnetism with high magnetic moment and optical properties of Co doped ZnO nanorods synthesized by a solvothermal route. *J. All. & Comp.* **615**, 378–385 (2014)
 34. K. Shomalian, M.-M. Bagheri-Mohagheghi, M. Ardyanian, Characterization and study of reduction and sulfurization processing in phase transition from molybdenum oxide (MoO_2) to molybdenum disulfide (MoS_2) chalcogenide semiconductor nanoparticles prepared by one-stage chemical reduction method. *Appl. Phys. A* **123**, 93 (2017)
 35. S. Singhal, J. Kaur, T. Namgyal, R. Sharma, Cu-doped ZnO nanoparticles: synthesis, structural and electrical properties. *Physica B* **407**, 1223–1226 (2012)
 36. V. Gandhi, R. Ganesan, H.H.A. Syedahamed, M. Thaiyan, Effect of cobalt doping on structural, optical, and magnetic properties of ZnO nanoparticles synthesized by coprecipitation method. *J. Phys. Chem. C* **118**(18), 9715–9725 (2014)
 37. T.M. Hammad, J.K. Salem, R.G. Harrison, Structure, optical properties and synthesis of Co-doped ZnO superstructures. *Appl. Nanosci.* **3**, 133–139 (2013)
 38. S. Bhattacharyya, A. Gedanken, Synthesis, characterization and room temperature ferromagnetism in cobalt-doped zinc oxide (ZnO:Co^{2+}) nanocrystals encapsulated in carbon. *J. Phys. Chem. C* **112**, 4517 (2008)
 39. V.K. Sharma, M. Najim, A.K. Srivastava, G.D. Varma, Structural and magnetic studies on transition metal (Mn, Co) doped ZnO nanoparticles. *J. Magn. Magn. Mater.* **324**, 683–689 (2012)
 40. S. Muthukumar, R. Gopalakrishnan, Structural, FTIR and photoluminescence studies of Cu Doped ZnO nanopowders by coprecipitation method. *Opt. Mater.* **34**, 1946–1953 (2012)
 41. A. Jagannatha Reddy, M.K. Kokila, H. Nagabhushan, R.P.S. Chakradhar, C. Shivakumar, J.L. Rao, B.M. Nagabhushan, Structural, optical and EPR studies on ZnO:Cu nanopowders prepared via low temperature solution combustion synthesis. *J. Alloys Compd.* **509**, 5349–5355 (2011)
 42. L. Vegard, Die konstitution der mischkristalle und die raumfüllung der atome. *Z. Phys* **5**, 17–26 (1921)
 43. N. Bahadur, A.K. Srivastava, S. Kumar, M. Deepa, B. Nag, Influence of cobalt doping on the crystalline structure, optical and

- mechanical properties of ZnO thin films. *Thin Solid Films* **518**, 5257 (2010)
44. P.K. Sharma, R.K. Dutta, A.C. Pandey, S. Layek, H.C. Verma, Effect of iron doping concentration on magnetic properties of ZnO nanoparticles. *J. Magn. Magn. Mater.* **321**(17), 2587–2591 (2009)
 45. P. Bhattacharyya, P.K. Basu, S. Basu, Fast response methane sensor using nanocrystalline zinc oxide thin films derived by sol-gel method. *Sens. Actuators B* **124**, 62–67 (2007)
 46. H.M. Jeong, H.J. Kim, P. Rai et al., Cr-doped Co_3O_4 nanorods as chemiresistor for ultra selective monitoring of methyl benzene. *Sens. Actuators B* **201**, 482–489 (2014)
 47. D.X. Ju, H.Y. Xu, Q. Xu, H.B. Gong, Z.W. Qiu, J. Guo, J. Zhang, B.Q. Cao, High triethylamine-sensing properties of NiO/SnO₂ hollow sphere P-N heterojunction sensors. *Sens. Actuators B* **215**, 39–44 (2015)